JOURNAL OF AIRCRAFT
Vol. 29, No. 6, Nov.-Dec. 1992

# Unsteady Simulation of Viscous Flowfield Around F-18 Aircraft at Large Incidence

Yehia M. Rizk*
*NASA Ames Research Center, Moffett Field, California 94035*
and
Ken Gee†
*MCAT Institute, Moffett Field, California 94035*

**This article describes the numerical simulation of the unsteady viscous flow around the F-18 aircraft at high angles of attack. A generalized overset zonal grid scheme is used to decompose the computational space around the complete aircraft, included deflected control surfaces. The grids around various components of the aircraft are created numerically using a three-dimensional hyperbolic grid generation procedure. The Reynolds-averaged Navier-Stokes equations are integrated using a time-accurate, implicit procedure. Results for the turbulent flow around the F-18 aircraft at 30 deg angle of attack show the details of the flowfield structure, including the unsteadiness created by the vortex burst and the resulting fluctuating airloads exerted on the vertical tail. The computed results agree fairly well with flight data for surface pressure, surface flow pattern, vortex burst location, and the dominant frequency for tail load fluctuations.**

## I. Introduction

EXTENSIVE research is currently being directed towards understanding the high-angle-of-attack flow regime with the objective of improving the high alpha performance of current and future aircraft. A validated data base is being obtained through flight, sub- and full-scale wind-tunnel testing and CFD simulation of the flow about the F-18 aircraft. The F-18 was selected as a base configuration because of its exceptional high-angle-of-attack capability. Flight testing and flow visualization is conducted at Ames-Dryden Flight Research Facility[1] using the high alpha research vehicle (HARV) that is a highly-instrumented F-18 aircraft (Fig. 1). Subscale wind-tunnel testing was conducted at Langley[2] and full-scale testing is currently being conducted at Ames. CFD simulation of the F-18 external flow is being performed at Ames[3-6] and Langley[7,8] while investigation of the internal flow through the inlet is being carried out at Lewis.[9] The objective of this paper is to describe a computational method for predicting the steady and unsteady external flowfield around the complete F-18 aircraft at large incidence. Emphasis is directed towards studying the inherent unsteadiness downstream of the vortex breakdown and the resulting unsteady loads on the twin vertical tails.

The task of simulating the flowfield around the F-18 represents a challenge to current CFD methods and computer resources because it involves both complicated physics and complex geometry. The complicated physics associated with high-angle-of-attack vortical flows involves massive separation, vortex interaction, vortex breakdown, and the resulting unsteadiness in the flowfield. The complex geometry of the F-18 represents a challenge to grid generation because of the many close-coupled components (e.g., wing and empennage) and the use of the control surfaces (leading- and trailing-edge flaps, and horizontal stabilator) to enhance the aircraft maneuverability. In addition, the wing leading-edge extension (LEX) generates a strong vortex that enhances the wing lift at high angles of attack. The twin vertical tails are canted to intercept the high energy flow in the vortex to increase their effectiveness. However, at moderate to high angles of attack, the LEX vortex bursts and induces buffeting to the tails. This tail buffeting phenomenon is not limited to the F-18, but has also been observed on other twin-tail fighters like the F-15. Both computational[10] and experimental[11] work on the F-15 indicates that tail buffeting occurs at moderate to high angles of attack.

The current numerical technique is based on the overset,[12] or Chimera[13,14] scheme. This technique acts as the framework for including the effects of different components of the aircraft. A generalized overset/patch zonal grid interfacing method[5,6] is added to the basic Chimera scheme to increase its range of application. The grids around the main components of the aircraft are created numerically using a three-dimensional hyperbolic[15,16] grid generation code. The equations governing fluid motion, represented by the Reynolds-averaged Navier-Stokes equations, are integrated using a partially upwind, two-factored procedure.[17]

The numerical method is briefly described in Sec. II, whereas the results and a comparison with flight data are described in Sec. III.

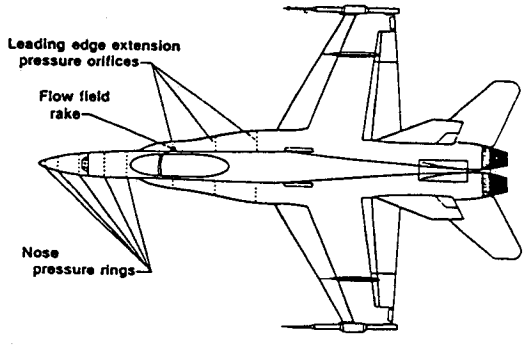


**Fig. 1 Top view of the F-18 HARV.**

Presented as Paper 91-0020 at the AIAA 29th Aerospace Sciences Meeting, Reno, NV, Jan. 7-10, 1991; received Jan. 31, 1991; revision received Nov. 4, 1991; accepted for publication Nov. 8, 1991. 

*Research Scientist. Associate Fellow AIAA.
†Research Scientist. Member AIAA.

## II. Numerical Method

The numerical simulation procedure is based on the use of the overset zonal scheme (Chimera) because of its considerable flexibility. The grid generation task is made easier because the scheme does not require neighboring grids to match along any common surface. Instead, it is simply required that two adjacent grids overlap each other. Moreover, overset grids become more attractive when simulating movable control surfaces scheduled with the angle of attack, or for flows where one grid is in relative motion with respect to the other grids.[18,19] Therefore, the overset scheme would be a suitable tool to extend the present work to couple the aerodynamic and structural response of a flexible tail due to buffeting. For complex junctions, such as fuselage-strake-wing, it would be advantageous to remove the requirement of overlap along body surfaces. Unlike overset grids, patch grids do not necessarily require grid overlapping, but they are generally more restrictive since they require zonal boundaries to match along common surfaces. For the current simulation, the generalized Chimera grid interfacing scheme[5,6] is used to maintain the flexibility of overset grids while relaxing the requirement of grid overlapping along body surfaces.

A three-dimensional body-fitted mesh can be generated numerically using the hyperbolic[15,16] procedure. The hyperbolic procedure has the desirable feature of allowing the user to specify an arbitrary point distribution along the body surface from which a body-normal grid is automatically created. Compared to other numerical grid generation procedures, the hyperbolic scheme is less costly in terms of computer time and memory, and the resulting grid can be made orthogonal or close to orthogonal everywhere. Since the grid is obtained by marching outward from the body surface, the hyperbolic scheme has a drawback in its inability to prescribe an exact location for the grid outer boundary. However, the use of the overset scheme does not require the exact matching of outer grid surfaces, thus, there is no need to specify an exact location for the outer boundary.

The nature of the separated flow in the high-angle-of-attack regime mandates the solution of the Navier-Stokes equations. A simpler set of equations, like the Euler equations, would not be suitable for simulating massively separated regions. Any Navier-Stokes code written for a single grid can be readily adapted to work with the overset scheme. The two-factored F3D code[17] was selected because it is implicit and can be run in either a time-accurate or steady-state mode. The F3D code has been used extensively in the past and validated for several viscous problems, including high-angle-of-attack flows.

### A. Geometry Definition and Approximations

It would be extremely difficult to model all the details of the F-18 geometry. Therefore, some simplifications are made to facilitate the simulation process. Small protuberances (e.g., antenna fairings), and small compounds (such as missile rails, etc.), are neglected because they are not expected to have a significant effect on the overall flowfield. The flow through the inlet is excluded in the current work. The use of overset gridding will allow the eventual inclusion of the internal flow through the engines by adding grids to simulate the inlet region and the exhaust plume.

The surface grid for the current computational model consists of the forebody, LEX, fair-over inlet, wing, deflected leading-edge flaps, vertical and horizontal tails, and an idealized boundary-layer divertor vent. The fuselage surface definition was given in terms of cross-sectional cuts. A fairing was added as shown in Fig. 2 to cover the inlet, and part of the boundary-layer divertor vent, and a sting was added to the back end of the computational model. The surface of the wing and the empennage are defined from given NACA cross sections with prescribed taper, twist, and thickness, etc. Since surfaces of different components were defined separately, some minor alterations were made to the fuselage, wing, and tails to ensure proper matching at the junctions. The leading-edge flap surface grid was obtained by deflecting the wing surface grid around the hinge line, that is located at the 20% chord position. A small spanwise gap (with thickness of about 0.005 chord) was assumed between the wing-root section and the flap-root section. The gap between the inboard and outboard flaps as well as any gaps along the hinge line are not simulated. The actual boundary-layer divertor vent geometry is very complicated. However to simulate the rough effect of the upward flow from underneath the LEX, an idealized boundary-layer divertor vent was created using approximate dimensions. The surface grid for the horizontal tail trim position was obtained by rotating the tail around its root midchord.

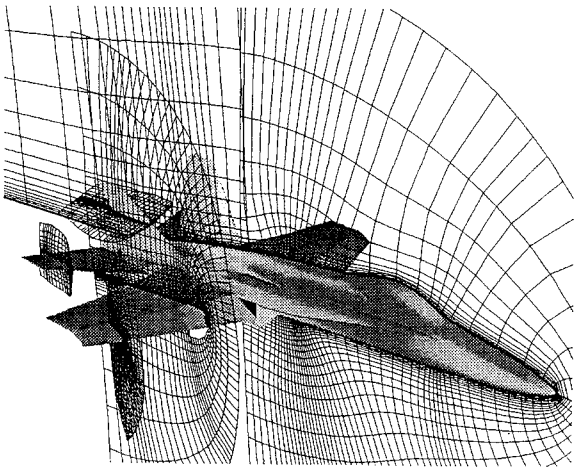

**Fig. 2 Overall view of the grid system.**

### B. Domain Decomposition

The main advantage of using the overset method is to reduce the grid generation procedure from the difficult task of creating a single grid around the entire configuration, to the simpler task of separately creating grids around relatively simpler components. Moreover, like other zonal methods, the overset method provides the capability to use different grid densities, different sets of governing equations, or different turbulence models in different regions, depending on physical considerations. In addition, zoning could be used to reduce the run-time computer core memory requirement through the use of auxiliary memory.

The grid system for the F-18 consists of 10 grids shown in Fig. 2. The fuselage (consisting of the forebody, LEX, faired-over inlet, aft end, and sting) is gridded separately from the other components. Furthermore, to reduce the memory requirement, two grids, instead of one, were created around the fuselage. Separate grids were created for the outer mesh, wing, flaps, gap between the fuselage and flaps, B. L. vent, horizontal and vertical tails. A detailed discussion of the grid system is given in Ref. 6. The hyperbolic grid generation code was used to generate the two fuselage grids, outer mesh, wing, flap, and tails grids. Special treatment for the sharp LEX leading edge, that uses one-sided differencing at discontinuities is discussed in Ref. 5. The horizontal tail grid was distorted near the tail root to make it coincide with the surface of the fuselage in a manner similar to that used in Ref. 20. The gap grid were created algebraically through transfinite interpolation from the wing and flap grids; similarly, the vent grid was created from the fuselage grid. Finally, communication among all interconnecting grids is established using the Pegasus code.[13]

### C. Governing Equations and Numerical Algorithm

For high-Reynolds-number flow, the use of body-fitted coordinates allows the thin-layer approximation in the outward direction to simplify the full Reynolds-averaged Navier-Stokes equations.[21,22] However, in order to treat nonbody-conforming grids and to maintain flexibility in zoning, the thin-layer approximation is extended to three directions. The governing

equations take the following form:

$$\partial_\tau \boldsymbol{Q} + \partial_\xi \boldsymbol{F} + \partial_\eta \boldsymbol{G} + \partial_\zeta \boldsymbol{H} = (\partial_\xi \boldsymbol{R} + \partial_\eta \boldsymbol{S} + \partial_\zeta \boldsymbol{T})/Re \quad (1)$$

where $\boldsymbol{Q}$ represents the dependent variable vector while $\boldsymbol{F}$, $\boldsymbol{G}$, and $\boldsymbol{H}$ are the inviscid flux vectors associated with the $\xi$, $\eta$, and $\zeta$ directions, respectively. The viscous terms in $\xi$, $\eta$, and $\zeta$ have been collected into the vectors $\boldsymbol{R}$, $\boldsymbol{S}$, and $\boldsymbol{T}$, respectively. In accordance with the thin-layer approximation, $\boldsymbol{R}$, $\boldsymbol{S}$, and $\boldsymbol{T}$ do not contain any cross-derivative terms.

The above equations are numerically integrated using the code F3D that is an implicit two-factored scheme that uses central differencing in the $\eta$ and $\zeta$ directions and upwind differencing in the $\xi$ direction. The discretized form of Eq. (1) takes the following form:

$$\begin{aligned}\mathcal{L}_f\mathcal{L}_b\Delta\boldsymbol{Q}^{n+1} = {} & -i_b\Delta t[\delta_\xi^b(\boldsymbol{F}^+)^n + \delta_\xi^f(\boldsymbol{F}^-)^n + \delta_\eta \boldsymbol{G}^n \\ & + \delta_\zeta \boldsymbol{H}^n - (\bar{\delta}_\xi \boldsymbol{R}^n + \bar{\delta}_\eta \boldsymbol{S}^n + \bar{\delta}_\zeta \boldsymbol{T}^n)/Re \\ & - (D_e|_\eta + D_e|_\zeta)\boldsymbol{Q}^n] \end{aligned} \quad (2)$$

where the forward and backward operators, $\mathcal{L}_f$, $\mathcal{L}_b$ are given by

$$\mathcal{L}_f = I + i_b[h\delta_\xi^b(\boldsymbol{A}^+)^n + h\delta_\zeta \boldsymbol{C}^n - hRe^{-1}\bar{\delta}_\zeta J^{-1} \cdot \boldsymbol{M}^\eta J - D_i|_\zeta]$$

$$\mathcal{L}_b = I + i_b[h\delta_\xi^f(\boldsymbol{A}^-)^n + h\delta_\eta \boldsymbol{B}^n - hRe^{-1}\bar{\delta}_\eta J^{-1}\boldsymbol{N}^n J - D_i|_\eta]$$

In Eq. (2), $h = \Delta t/\varepsilon$ where $\varepsilon = 1$ for first-order and $\varepsilon = 2$ for second-order time accuracy, and $\Delta t$ is the time step. Also, in Eq. (2), $\delta$ is a three-point second-order accurate central difference operator, while $\bar{\delta}$ is a midpoint operator used with the viscous terms. The flux $\boldsymbol{F}$ associated with the $\xi$ direction has been eigensplit allowing the use of backward and forward difference operators $\delta_\xi^b$ and $\delta_\xi^f$. This differencing maintains the freestream divergence in general curvilinear coordinates when coupled with consistently differenced centered metrics. The $5 \times 5$ matrices $\boldsymbol{A}$, $\boldsymbol{B}$, $\boldsymbol{C}$, $\boldsymbol{M}$, and $\boldsymbol{N}$ result from local linearization of the fluxes about the previous time level.

The dependent variable vector $\boldsymbol{Q}^{n+1}$ is obtained from the above two-factored algorithm by solving the following sequence at each time step, one grid at a time:

$$\begin{aligned} \mathcal{L}_f\Delta Q^* &= \text{RHS} \\ \mathcal{L}_b\Delta\boldsymbol{Q}^{n+1} &= \Delta Q^* \\ \boldsymbol{Q}^{n+1} &= \boldsymbol{Q}^n + \Delta\boldsymbol{Q}^{n+1} \end{aligned} \quad (3)$$

where RHS is the right-hand side of Eq. (2). The only difference between Eq. (2) and the F3D algorithm, as applied to single-block grids, is in the use of the three-dimensional array $i_b$, that is introduced to allow the use of overset grids without affecting the code vectorization. This parameter is set either to one (at regular field points) or zero (at boundary or hole points). It is obvious that when $i_b$ is equal to one, Eq. (2) reduces to the original F3D algorithm. However, at boundary or hole points, $i_b$ is set to zero, and the integration scheme reduces to $\boldsymbol{Q}^{n+1} = \boldsymbol{Q}^n$. Thus, $\boldsymbol{Q}$ is not updated by the numerical integration procedure at boundary or hole points. The boundary points are updated at the end of each time step by the physical and grid interfacing boundary conditions. Hole points do not need to be updated, and can remain at their initial (freestream) conditions without affecting the rest of the flowfield. However, because of the way the turbulence models work, blanked-out hole points are updated at the end of each step by either interpolation or extrapolation from nearby field points.

The explicit and implicit dissipation operators, $D_e$ and $D_i$, are used in the $\eta$ and $\zeta$ directions to suppress high frequencies associated with central differencing. The explicit smoothing is a blend of fourth- and second-order terms, whereas the implicit smoothing consists of only second-order terms. Details of the smoothing terms and how they are modified for the Chimera scheme to switch from fourth order to second order near blanked-out regions is given in Ref. 14.

For time-accurate calculations, $\Delta t$ is the same for all grid points, while for steady-state calculations, local time stepping is used to speed up the convergence by allowing $\Delta t$ to vary from point-to-point according to a function of the Jacobian of the coordinate transformation, $J$. Such a variation results in using values of $\Delta t$ of the order one away from the body surface, and $\Delta t$ of the order 0.01 near the body surface, where the mesh spacing is finest.

It must be noted that even though Eq. (1) contains the viscous terms in all directions, most grids are body-fitted, and only the viscous terms in the direction associated with the normal direction, $\zeta$, are retained. The viscous terms are implemented implicitly in the $\eta$ and $\zeta$ directions. However, due to limitation in F3D, the viscous terms can only be treated explicitly in the upwind, $\xi$, direction.

### D. Boundary Conditions

There are two types of boundary conditions in the F3D/Chimera scheme. The first type deals with physical boundaries, while the second type deals with grid communication as a result of domain decomposition. Both types of boundary conditions are explicitly imposed.

The physical boundary conditions are enforced with calls to modular routines. Various grid topologies are treated through input control parameters to the code. The boundary conditions include viscous wall conditions that could be applied on one or more sides of the computational domain. Also, outflow, axis-averaging, wing-cut-averaging, or symmetry boundary conditions can be enforced on any boundary surface or a subset of it.

For the grid interface boundary conditions, trilinear interpolation across zones is used to obtain the flow variables at boundary points resulting from domain decomposition (outer boundary points or hole boundary points). Boundary points could lie within the field points of another grid (overset mode) or on the boundary of another grid (patch mode). In both modes, three-dimensional interpolation is used to maintain generality. In the patch mode, the interpolated values are averaged with a zero-order extrapolation from the interior domain. This boundary condition is similar to what is commonly used to simulate, e.g., a wing-cut. Based on a numerical experimentation in Ref. 6, communication is done in a patch mode when the overlap is zero, while communication in overset mode is used for overlap values greater than half a cell size. A weighted average is used for overlap ratios between zero and half a cell size.

In the current work, trilinear interpolation is used. The use of the explicit trilinear boundary conditions has proven to be adequate in previous applications.[13,14] Higher order interpolation scheme (tricubic) has been used[20] in order to reduce interpolation errors, however, it requires bigger overlap regions.

If interpolation is applied on the $Q$ variable, this would not ensure conservation. However, if interpolation is applied on $\Delta Q$, it could be shown that conservation is maintained.[23] Numerical experimentation has shown that the $\Delta Q$ interpolation is slightly more accurate in the presence of shocks. In the absence of shocks, the two schemes produce very similar results. The $\Delta Q$ interpolation requires consistent initial and restart conditions. Therefore, in the current applications, interpolation is applied on $Q$ for simplicity.

### E. Turbulence Modeling

In the current work, computations are carried out at actual flight conditions. Flight Reynolds numbers produce turbulent flow over the majority of the airplane, with the exception of small laminar and transitional regions near the nose. There-

fore, in the current computations, this small region is neglected and the computations are performed, assuming the flow to be fully turbulent.

There is no universal model that could be used to simulate the turbulence on all parts of the aircraft, due to the difference in physics in each region. The algebraic turbulence model of Baldwin and Lomax[22] has been proven to be simple and fairly accurate for attached boundary-layer flow. Different modifications to this widely used model are available. An example of this is the Degani-Schiff[24] modification to account for crossflow separation. As mentioned before, zonal schemes allow the use of different turbulence models in different zones.

The flow on the LEX is dominated by the effects of the sharp leading edge, that fixes the location of the primary crossflow separation line. This means that, the flow in the LEX region will not be too sensitive to the turbulence model. However it is important to use the crossflow separation modification of Ref. 24 on the forebody because the flow there is more sensitive to the turbulence model. The LEX vortex inhibits flow separation on the majority of the upper side of the wing; therefore, the use of Baldwin-Lomax model would be justified. However, the outer-layer search cut-off distance was set to a small value in a manner similar to Panaras and Steger[25] to make sure that the high vorticity in the LEX vortex does not result in a high turbulent eddy viscosity on the upper side of the wing.

A crude turbulence model was devised to be used in the gap region between the LEX and wing leading-edge flap and inside the boundary-layer divertor vent. This model uses the Baldwin-Lomax model on two opposite walls. A blending function was used to smooth out the variations of the eddy viscosity in the middle of the two walls; no modification for corner regions was used. In the future, other models will be tried, however, for the time being, only the rough effects of the flow inside the gap and vent on the overall flowfield are being simulated.

The use of the Chimera scheme with models based on the Baldwin-Lomax eddy-viscosity model could create problems if the flow variables inside the holes are kept at their free-stream values. This is especially true if a hole is close to a body surface and the search process for the maximum function that determines the outer-layer eddy viscosity encounters rapid changes in the flowfield across hole boundaries. This may produce erroneous values for the turbulent viscosity. In the current work, this was cured by using linear interpolation to fill the blanked-out hole points.

## III. Results

The present numerical procedure was used to compute the turbulent flow around the F-18 at a Mach number of 0.243, an angle of attack 30.3 deg, and a Reynolds number (based on the wing mean aerodynamic chord) of $11 \times 10^6$. These conditions were selected to correspond to flight-test conditions of the HARV. At this angle of attack, the inboard and outboard leading-edge flaps are deflected 33 deg nose down

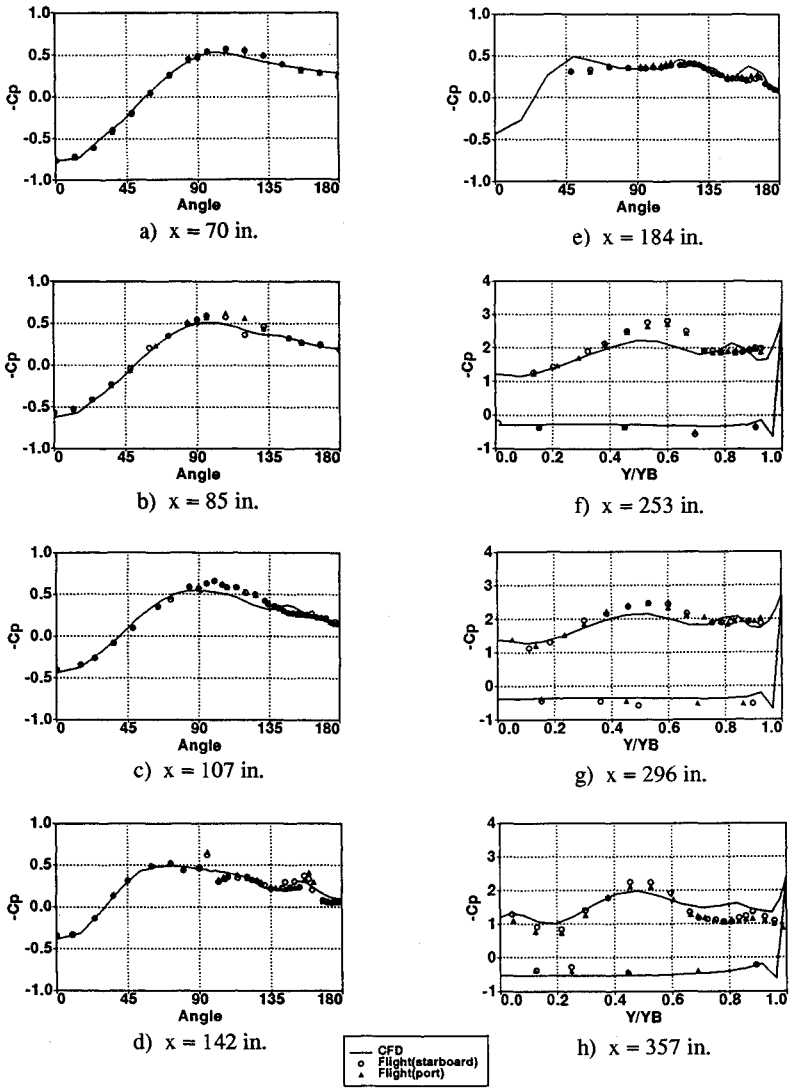


**Fig. 3 Cp comparison between computations and fight data.**

and the horizontal tail is deflected 7 deg nose down. Bilateral symmetry was assumed and 10 grids consisting of a total of about 0.9 million points around half the configuration were used. For all the grids, the normal spacing near the wall were chosen to be small enough to keep the average value of $y^+$ less than 5 along the majority of the body surface. The code was run in the nontime-accurate mode for 1000 steps and in a time-accurate mode for an additional 8600 time steps using the first-order temporal accurate option. The solution required less than 8 MV of core memory and about 40 s per time step on the CRAY-YMP.

The computed surface-pressure distributions are compared to the HARV flight-test data[1] in Fig. 3. The first five stations shown are located on the fuselage forebody, whereas the last three stations are on the LEX (Fig. 1). It is seen that there is fairly good agreement between the computations and flight data. The computation tends to predict a local suction peak at around 145 deg at station three. This peak starts to show up in the flight data at station four, where the comparison is better. The early prediction of this pressure peak is probably due to the lack of a transition model in the current turbulence model. The discrepancy at station four at about 95 deg is due to antenna fairings on the HARV. It is obvious that the effect is local and does not affect the flowfield elsewhere. The pressure coefficient comparison on the LEX shows good agreement. However, there are some differences on the upper side of LEX where the computations underpredict the suction peak due to the LEX vortex at station 6 and to a lesser extent at station 7. The computations do a good job in predicting the drop in the suction peak at station 8 due to the vortex burst. It must be noted that, in a previous work,[5] detailed comparison of coarse-mesh and fine-mesh solutions around a simplified F-18 indicates that the coarse grid does a fairly good job in predicting the overall features of flowfield; the fine mesh predicts a stronger LEX vortex. Therefore, the surface-pressure suction peaks are predicted better by the fine mesh.

The overall pressure distribution along the body surface is shown in Fig. 4. Figure 5a shows a flight photo of the LEX vortex as visualized with smoke and the surface flow pattern visualized with the tufts. The numerical solution in Fig. 5b shows the instantaneous particle traces and limiting-surface streamlines on the LEX, wing, and deflected leading-edge flaps. There is good agreement between the computations and the flight test for the LEX vortex burst location and surface flow pattern.

Both flight data and computations indicate that the flow is steady (ahead of the burst point). However, the burst-point location and the spiral flow structure downstream is highly unsteady. This unsteady flowfield of the burst vortex generates an unsteady loading on the vertical tail as seen from the history of the tail total bending moment in Fig. 6. This time history was obtained by using a constant time step of 0.005.

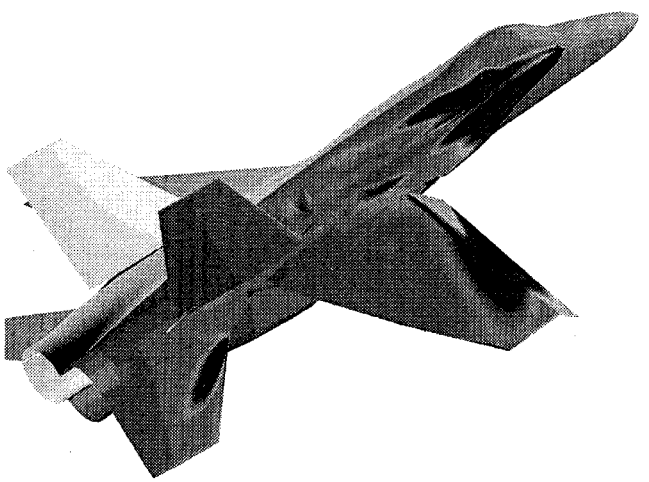

Fig. 4 Computed surface pressure.

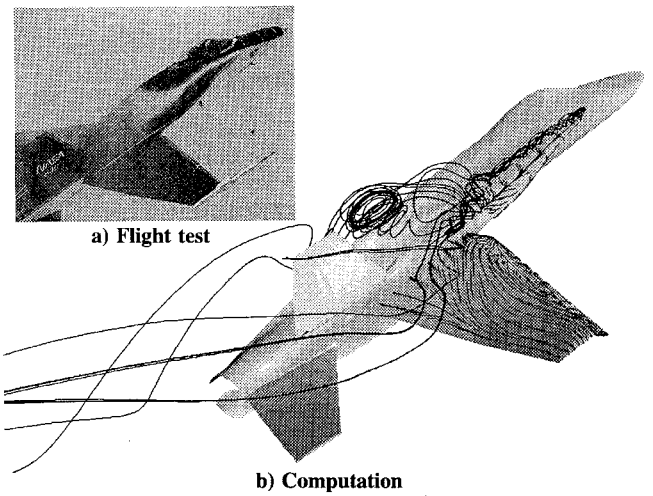


Fig. 5 Particle traces and surface flow pattern.

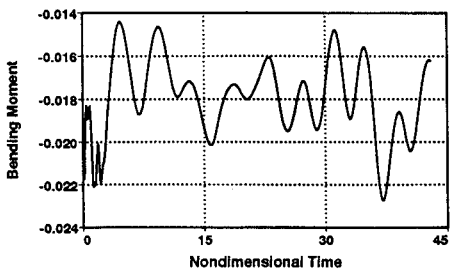


Fig. 6 Time history of vertical tail total bending moment.

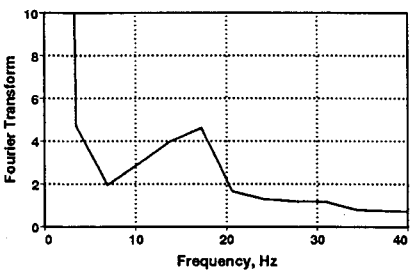


a) 4096 steps.

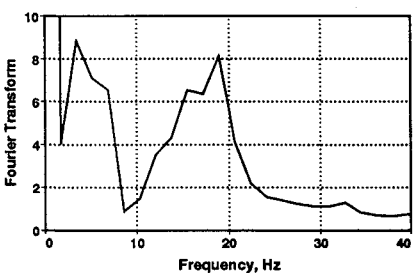


b) 8192 steps.

Fig. 7 Fourier transform of the vertical tail total bending moment.

This value of time-step was determined by stability and is nondimensionalized based on wing-root chord and freestream speed of sound. Figure 6 indicates that after an initial transient, the time history shows a pattern of near periodic fluctuations.

In order to study the frequency content of the unsteadiness, a fast Fourier transform was performed after each $2^n$ steps, where $n$ is an integer. The Fourier transforms for two consecutive intervals corresponding to 4096 steps ($n$ = 12) and 8192 steps ($n$ = 13) are shown in Fig. 7. This corresponds to intervals of about 0.29 and 0.58 seconds of actual time, respectively. Both intervals yield a dominant frequency in the range of 15–20 Hz. It is also seen that increasing the interval reveals an additional low-frequency and a wider-frequency

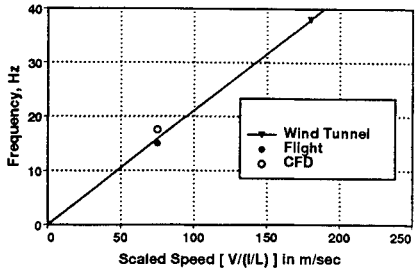


**Fig. 8 Comparison between predicted and measured frequency.**

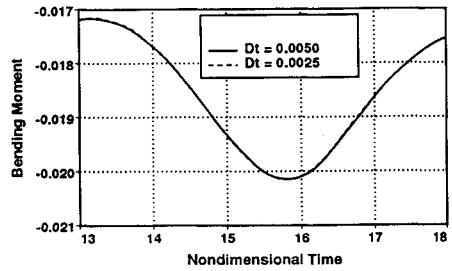


**Fig. 9 Effect of time-step on vertical tail load history.**

band centered around the dominant frequency. It is obvious that carrying out the computations further will give a better definition of the low frequency. It must be noted that the first natural frequency of the vertical tail[26] is 15 Hz (first bending mode). Therefore, tail buffeting is induced because the airloads dominant frequency is very close to the first natural frequency of the tail. The additional low frequency is not expected to play a significant role in buffeting because it is considerably less than the lowest natural frequency.

Figure 8 shows a comparison between the predicted airloads frequency and the frequency measured by subscale wind-tunnel[27] and HARV flight test[28,29] at angles of attack of about 30 deg. The wind-tunnel frequency was obtained using pressure transducers and represents the induced unsteady airloads frequency. The flight frequency was obtained from an accelerometer and represents the structural response of the vertical tail. The wind-tunnel data shows that the frequency is linearly proportional to the tunnel speed. The tunnel speed was scaled to the full-scale dimensions to allow for comparison with flight data and CFD. The comparison shows that there is good agreement between the computations, wind tunnel, and flight data.

Finally, in order to check the time accuracy of the code, the time step was reduced from 0.005 to 0.0025 and the computations were repeated for about five nondimensional time units. Figure 9 shows that reducing the time step does not alter the time history, indicating that the time variations are being well-resolved and no higher frequencies are present. Therefore, the relatively coarse mesh used in the present study, allowed the analysis of the unsteadiness created by the vortex burst and revealed that the dominant load fluctuating frequency is in the range of excitation of structure modes of the tail.

## IV. Conclusions

A numerical procedure for simulating the unsteady flow around the F-18 aircraft at high angles-of-attack was outlined. This method employs a generalized overset zonal scheme that has the flexibility needed for zoning a complex configuration like the F-18. Time-accurate computations were performed to examine the unsteady nature of the flowfield downstream of the vortex breakdown point, and the resulting unsteady loads on the vertical tail. A Fourier analysis revealed that the dominant frequency is very close to the first natural frequency of the tail. The predicted frequency agrees fairly well with measured frequency. This work represents the first step in studying the tail buffet phenomenon computationally, and will be extended to include the structure response of a flexible vertical tail.

## Acknowledgments

The authors thank Lewis Schiff of NASA Ames Research Center for helpful discussions.

## References

[1]Fisher, D. F., Banks, D. W., and Richwine, D. M., "F-18 High Alpha Research Vehicle Surface Pressure: Initial In-Flight Results and Correlation With Flow Visualization and Wind Tunnel Data," NASA TM 101724, 1990.

[2]Erickson, G. E., Hall, R. M., Banks, D. W., Del Ferate, J. H., Schreiner, J. A., Hanley, R. J., and Pulley, C. T., "Experimental Investigation of the F/A-18 Vortex Flows at Subsonic Through Transonic Speeds," AIAA Paper 89-2222, Aug. 1989.

[3]Schiff, L. B., Cummings, R. M., Sorenson, R. L., and Rizk, Y. M., "Numerical Simulation of High Incidence Flow over the F-18 Fuselage Forebody," AIAA Paper 89-0339, Jan. 1989.

[4]Cummings, R. M., Rizk, Y. M., Schiff, L. B., and Chaderjian, N. M., "Navier-Stokes Predictions of the Flowfield Around the F-18 (HARV) Wing and Fuselage at Large Incidence," AIAA Paper 90-0099, Jan. 1990.

[5]Rizk, Y. M., Schiff, L. B., and Gee, K., "Numerical Simulation of the Viscous Flow Around a Simplified F/A-18 At High Angles of Attack," AIAA Paper 90-2999, Aug. 1990.

[6]Rizk, Y. M., and Gee, K., "Numerical Prediction of the Unsteady Flowfield Around the F-18 Aircraft at Large Incidence," AIAA Paper 91-0020, Jan. 1991.

[7]Thomas, J. L., Walters, R. W., Reu, T., Ghaffari, F., Weston, R. P., and Luckring, J. M., "A Patched Grid Algorithm for Complex Configurations Directed Towards the F/A-18 Aircraft," AIAA Paper 89-0121, Jan. 1989.

[8]Ghaffari, F., Luckring, J., Thomas, J., and Bates, B., "Navier-Stokes Solution about the F/A-18 Forebody-LEX Configuration," AIAA Paper 89-0338, Jan. 1989.

[9]Burley, R., Anderson, B. H., Smith, C., and Harloff, G., "High Alpha Inlets—A Perspective," NASA High Angle of Attack Technology Conf., Hampton, VA, Oct. 31–Nov. 1, 1990.

[10]Sankar, N. L., and Kwon, O. J., "High Alpha Simulation of Fighter Aircraft," NASA High Angle of Attack Technology Conf., Hampton, VA, Oct. 31–Nov. 1, 1990.

[11]Komerath, N. M., McMahoan, H. M., Schwartz, R. J., Liou, S. G., and Kim, J. M., "Unsteady Flow Field Measurements Near a Fighter Model at High Angles of Attack," AIAA Paper 90-1431, June 1990.

[12]Atta, E. H., "Component Adaptive Grid Interfacing for Three Dimensional Transonic Flows About Aircraft Configuration," AIAA Paper 81-0382, Jan. 1981.

[13]Benek, J. A., Steger, J. L., Dougherty, F. C., and Buning P. G., "Chimera: A Grid Embedding Technique," Arnold Engineering Development Center TR-85-64, Arnold AFS, TN, 1986.

[14]Buning, P. G., Chiu, I. T., Obayashi, S., Rizk, Y. M., and Steger, J. L., "Numerical Simulation of the Integrated Space Shuttle Vehicle in Ascent," AIAA Paper 88-4359, Aug. 1988.

[15]Steger, J. L., and Rizk, Y. M., "Generation of Three Dimensional Body Fitted Coordinates Using Hyperbolic Partial Differential Equations," NASA TM 86753, June 1985.

[16]Rizk, Y. M., Steger, J. L., and Chaussee, D., "Use of Hyperbolic Grid Generation Scheme in Simulating Supersonic Viscous Flow About Three Dimensional Winged Configurations," *International Symposium on Computational Fluid Dynamics*, Tokyo, Sept. 9–12, 1985, pp. 995–1006.

[17]Ying, S. X., Steger, J. L., Schiff, L. B., and Baganoff, D., "Numerical Simulation of Unsteady, Viscous, High Angle of Attack Flows Using a Partially Flux-Split Algorithm," AIAA Paper 86-2179, Aug. 1986.

[18]Meakin, R. L., and Suhs, N., "Unsteady Aerodynamic Simulation of Multiple Bodies in Relative Motion," AIAA Paper 89-1996, June 1989.

[19]Dougherty, F. C., Benek, J. A., and Steger, J. L., "On Application of the Chimera Grid Scheme to Store Separation," NASA TM 88193, Oct. 1985.

[20]Yarrow, M., and Mehta, U. B., "Multiprocessing on Supercomputers For Computational Aerodynamics," NASA TM-102806, May 1990.

[21]Steger, J. L., "Implicit Finite-Difference Simulation of Flow About

Arbitrary Two-Dimensional Geometries," *AIAA Journal*, Vol. 16, July 1978, pp. 679–686.

[22]Baldwin, B. S., and Lomax, H., "Thin Layer Approximation and Algebraic Model for Separated Turbulent Flow," AIAA Paper 78-257, Jan. 1978.

[23]Steger, J. L., Private communication, Aug. 1990.

[24]Degani, D., and Schiff, L. B., "Computation of Turbulent Supersonic Flows Around Pointed Bodies Having Crossflow Separation," *J. Comp. Phys.*, Vol. 66, Sept. 1986, pp. 173–196.

[25]Panaras, A. G., and Steger, J. L. "A Thin-Layer Solution of the Flow About a Prolate Spheroid," *Z. Flugwiss, Weltraumforsch.*, Vol. 12, No. 3, 1988, pp. 173–180.

[26]Graham, A. D., and Watters, K. C., "Full Scale Fatigue Testing of the F/A-18 Empennage," The Australian Aeronautical Conf., Melbourne, Australia, Oct. 1989.

[27]Martin, C. A., and Thompson, D. H., "Scale Model Measurements of Fin Buffet Due to Vortex Bursting on F/A-18," AGARD Fluid Dynamics Specialists Meeting, Toulouse, France, Paper 12, 1991, pp. 12.1–12.10.

[28]Del Frate, J. H., Freudinger, L. C., and Kehoe, M. W., "F-18 Tail Buffet," High Alpha Technology Program Workshop, Dryden Flight Research Facility, Edwards, CA, 1989.

[29]Lee, B., Brown, D., Zgela, M., and Poirel, O., "Wind Tunnel Investigations and Flight Tests of Tail Buffet on the CF-18 Aircraft," *AGARD Specialists Meeting on Aircraft Dynamic Loads*, Sorrento, Italy, April 1990, pp. 1.1–1.20.